Molecular MRI for sensitive and specific detection of lung metastases

Rosa T. Branca[a,1], Zackary I. Cleveland[b], Boma Fubara[b], Challa S. S. R. Kumar[c], Robert R. Maronpot[d], Carola Leuschner[e], Warren S. Warren[a], and Bastiaan Driehuys[b]

[a]Center for Molecular and Biomolecular Imaging, Department of Chemistry, Duke University, Durham, NC 27708; [b]Center for In Vivo Microscopy, Department of Radiology, Duke University Medical Center, Durham, NC 27710; [c]Center for Advanced Microstructures and Devices, Louisiana State University, Baton Rouge, LA 70806; [d]Experimental Pathology Laboratories, National Institute of Environmental Health Sciences, Raleigh, NC 27709; and [e]Pennington Biomedical Research Center, Baton Rouge, LA 70808

Communicated by William Happer, Princeton University, Princeton, NJ, January 14, 2010 (received for review June 9, 2009)

Early and specific detection of metastatic cancer cells in the lung (the most common organ targeted by metastases) could significantly improve cancer treatment outcomes. However, the most widespread lung imaging methods use ionizing radiation and have low sensitivity and/or low specificity for cancer cells. Here we address this problem with an imaging method to detect submillimeter-sized metastases with molecular specificity. Cancer cells are targeted by iron oxide nanoparticles functionalized with cancer-binding ligands, then imaged by high-resolution hyperpolarized ^{3}He MRI. We demonstrate in vivo detection of pulmonary micrometastates in mice injected with breast adenocarcinoma cells. The method not only holds promise for cancer imaging but more generally suggests a fundamentally unique approach to molecular imaging in the lungs.

hyperpolarized gas MRI | superparamagnetic iron oxide nanoparticles | luteinizing hormone-releasing hormone

In 2009, ≈1,400,000 people in the United States were diagnosed with cancer, and as many as 562,000 died of the disease (1). Despite impressive increases in the number of cancer drugs and treatments, cancer survival rates have remained low for the past 20 years. Survival in cancer patients depends strongly on cancer containment and is thus inversely correlated with the incidence of metastases (2). Although all of the causes are not fully known, cancer metastases are particularly opportunistic in the lungs and are found in 20–54% of all patients who die of the disease (3). Because the presence of lung metastases will alter cancer management, their early and specific identification could provide a timely and powerful tool for improving patient outcomes.

Detection of lung metastases by current preclinical or clinical imaging techniques has substantial limitations. X-ray computed tomography (CT) permits clinical imaging of pulmonary nodules as small as 1 to 2 mm but lacks the specificity to distinguish benign lesions from cancerous tumors (4, 5). Positron emission tomography with fluorodeoxyglucose (FDG-PET) can differentiate between benign and cancerous lesions, but its low spatial resolution limits its use and reduces its specificity for malignancy in lesions smaller than 5 mm (6, 7). Moreover, both modalities use ionizing radiation, which represents a serious concern in repeated scanning, particularly in young adult patients and children (8). An equally compelling need exists for new preclinical molecular imaging of xenograft murine models. Although they replicate human disease imperfectly, these models provide an expeditious means to explore the biologic determinants of metastases and evaluate novel therapies, while readily permitting histologic correlation. Such preclinical studies would benefit equally from noninvasive longitudinal imaging with better resolution than current methods (≈1.2 mm detection limit for PET and 0.85 mm for micro-CT (9).

Here, we introduce a fundamentally unique, minimally invasive, and specific approach to cancer detection in the lung by combining two MRI technologies—hyperpolarized (HP) ^{3}He and functionalized superparamagnetic iron oxide nanoparticles (SPIONs). SPIONs are a particularly promising class of MR contrast agents, because they generate strong local magnetic susceptibility gradients that rapidly dephase nearby transverse magnetization and thereby produce localized dark spots in an MR image (10–12). Their effect is so strong that a small number of SPION particles can dephase a large number of surrounding spins, allowing even single cells to be detected (13, 14). Different versions of these iron oxide particles (10–100 nm in size) are commercially available and are used to image tumors in the liver and to detect metastasic invasion of lymph nodes (15). Moreover, this contrast agent can be easily functionalized with biologically active ligands to endow them with a high degree of molecular targeting specificity (16, 17). Size and coating are, in this case, key factors to escape macrophage recognition and to improve targeting efficacy (16). Although functionalized SPIONs are not yet approved for clinical use, a great variety of particles have been shown to accumulate selectively in cancer cells (17).

MRI is a well-established diagnostic tool for studying most organs, but this imaging modality is particularly challenged by the lung. The lung's tissues constitute only 20–25% of the total lung volume, and in the gas exchange regions this density is reduced to 10% (18). The lung's low density thus generates weak intrinsic MRI signals, but more importantly, its many air–tissue interfaces give rise to substantial field gradients (a few mT/m at 2 T), such that the small available tissue signal decays rapidly with a T_2^* on the order of 1 ms for humans at 1.5 T (19) and <0.8 ms for small animals at 2.0 T (20). This rapid decay makes it virtually impossible to observe any additional ^{1}H spin dephasing caused by SPIONs in the lung. Fortunately, the recent innovations of HP ^{3}He and ^{129}Xe MRI now permit high-resolution imaging of the lung both clinically (21–25) and preclinically (26–29). The low density of these gases is overcome by increasing their nuclear polarization by 4 to 5 orders of magnitude through laser-based optical pumping techniques (30). Unlike immobilized tissue protons, these gases are much less affected by the lung's susceptibility gradients because their high diffusivity averages away most of the field gradients experienced at the alveolar walls. This motional narrowing gives the HP gases a transverse relaxation time in the native lungs that is much longer than that of protons [$T_{2,Xe}^*$ ≈50.4 ms (31), $T_{2,\ He}^*$ ≈26.8 ms in humans at 1.5 T (32)], providing a much longer temporal window for SPIONs to induce dephasing.

SPIONs generate a magnetic field gradient that induces a broad phase spread in the transverse magnetization of the HP gases. Although motional narrowing may still average out this dephasing in a single alveolus, the averaging cannot extend across multiple alveoli. This causes a transition to the static dephasing regime and

Author contributions: R.T.B. and B.D. designed research; R.T.B., Z.I.C., B.F., and B.D. performed research; C.S.S.R.K., C.L., and W.S.W. contributed new reagents/analytic tools; R.T.B. and R.R.M. analyzed data; and R.T.B., and B.D. wrote the paper.

Conflict of interest statement: R.T.B and B.D. are inventors on a pending patent application relating to the technology described in this article. B.D. receives royalties for several patents related to hyperpolarized gas MRI.

[1]To whom correspondence should be addressed. E-mail: tamara.branca@duke.edu.

to a macroscopic signal loss similar to that produced by an aggregation of magnetically labeled cells in tissue (33), with a signal decay more likely proportional to the square of the echo time (TE). The long T_2^* of the HP gases in the native lung permit images to be acquired at longer TE than for ^{1}H MRI, thereby permitting dephasing of a larger surrounding volume of the magnetization. Combined with the high spatial resolution and signal-to-noise ratio (SNR) with which the lung can be imaged using HP gases, they provide an ideal medium with which to detect SPION contrast.

The use of untargeted iron oxide particles, injected intravenously, has already been shown to alter the ^{3}He MRI scan contrast in relation to pulmonary perfusion (34). In this work, we expand on this mechanism by using SPIONs functionalized with luteinizing hormone–releasing hormone (LHRH) to selectively target breast cancers that have metastasized to the lung. LHRH-SPIONs have previously been demonstrated to have low affinity for healthy lung tissue but to accumulate by receptor-mediated endocytosis in lung metastases (72 pg of Fe per cell) that overexpress the LHRH receptor (35). These particles, which have an uncoated size of 12 nm and a hydrodynamic size smaller than 50 nm, are designed for prolonged circulation (more than 12 h of plasma life time) and low opsonization that permits the LHRH-SPIONs to escape macrophage recognition (35). After injection, LHRH-SPIONs accumulate in metastatic cancer cells, forming clusters smaller than 0.5 μm (35) that can then be detected using HP ^{3}He MRI.

In this study, we examined the lungs of nude mice inoculated orthotopically, in the mammary fat pads, with human breast adenocarcinoma (MDA-MB-231, $n = 4$), or s.c. with either human breast carcinoma cells (MDA-MB-435s, $n = 4$) or prostate cancer cells (PC3, $n = 4$). Subcutaneous inoculations of these cancer cell lines in nude mice usually produce a low rate of pulmonary metastases, whereas orthotopic implantations result in a higher rate (36). The metastases, when present, are targeted by LHRH-SPIONs with equal affinity as the primary tumor (35, 37). To detect these metastatic nodules using our protocol, the animals were imaged using HP ^{3}He 24–48 h after an i.p. injection of LHRH-SPIONs (Fig. 1). Intraperitoneal rather than i.v. injections were used to avoid the possibility of SPION cluster aggregation in the pulmonary capillary beds, which could generate false-positive image findings. Immediately after the MRI experiments, the mice were killed by an overdose of pentobarbital, and their lungs were processed for histopathology to identify tumor sites and to provide a gold standard against which ^{3}He MRI could be compared.

Results

A convenient method for demonstrating SPION-induced dephasing of ^{3}He MRI in the lung is to exploit the nonspecific uptake of SPIONs in the right cranial mediastinal lymph node, which sits directly under the right cranial lobe of the lung. This uptake is caused by the drainage of the nanoparticles from the i.p. cavity to the lymphatic system (38). When the contrast agent is administrated i.p., some of the SPIONs accumulate into the right cranial mediastinal lymph node and produce a strong susceptibility effect that dephases the ^{3}He spins in the nearby lung parenchyma, causing a local signal loss. An example is shown in Fig. 2: the top row (Fig. 2*A*) shows a control animal that received no SPIONs, whereas the middle row (Fig. 2*B*) shows an animal with SPIONs in the lymph node and the associated ^{3}He signal attenuation. The presence of iron in the lymph node was confirmed by histologic examination, as shown in Fig. 2 *D* and *E*. Iron in this lymph node was detected by ^{3}He MRI in all tumor-bearing animals that did not develop lung metastases. Histologic examination of the healthy lung tissues in all animals revealed no iron and indicates that these particles escaped recognition by the lung macrophages, consistent with prior studies (35).

The nonspecific SPION uptake in the lymph node was also used to demonstrate the enhancement of SPION contrast with increasing TE. Fig. 3 shows that, although some ^{3}He signal attenuation is already observable at short TE (1 ms), it is significantly enhanced at longer TE (4 ms). This pattern was observed in all experiments, indicating that the sensitivity of this technique (i.e., the contrast-to-noise ratio) is enhanced at longer TE. Moreover, the signal void seen on ^{3}He MRI is larger than the actual cluster of iron particles that gives rise to it. In this example, the SPIONs were found to be loosely clustered over a 300-μm area but gave rise to a signal void with a 1,200-μm diameter on ^{3}He imaging.

Fig. 4 shows an example of 3D radial ^{3}He images acquired at TE = 4 ms from a control animal and from a mouse bearing a human breast adenocarcinoma xenograft, after the injection of the LHRH-SPION. Whereas the control animal showed high signal intensity throughout the lungs, the tumor-bearing animal showed a pronounced signal loss that affected the entire right lung. Comparison of ^{3}He MRI against H&E histology confirmed that ^{3}He signal voids occurred in the region of the lung parenchyma that contained disseminated micrometastases (Fig. 5*A*). Additionally, Prussian blue staining revealed that these micrometastases had been heavily targeted by LHRH-SPIONs (Fig. 5*C*). Further immunohistochemical staining confirmed that SPIONs did not accumulate in healthy lung tissue (Fig. 5*D*), which are free of LHRH receptors (Fig. 5*F*), but were confined to cancer cells with high LHRH receptor expression (Fig. 5 *E–H*).

Discussion

This study demonstrates that HP ^{3}He MRI combined with a targeted SPION contrast agent can detect early-stage metastatic lung tumors in mice. The SPION particles specifically target micrometastases in the lung parenchyma, which are then detec-

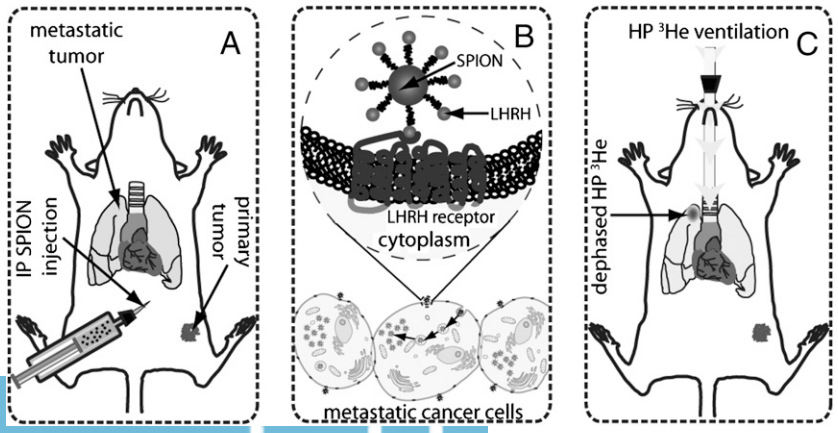

Fig. 1. Diagram illustrating the detection of breast and prostate cancer metastases in a mouse lungs. (*A*) Forty-eight hours before the imaging session, mice receive an i.p. injection of LHRH-SPIONs. (*B*) Cancer cells overexpressing LHRH receptors on their cell membrane take up LHRH-SPIONs through receptor-mediated endocytosis, causing SPIONs to accumulate in the cell, where they form submicron-sized clusters. (*C*) The iron uptake is then detected using HP ^{3}He MRI. HP ^{3}He transverse magnetization is rapidly dephased by SPIONs that have clustered in the metastatic lesions. As a result, metastatic nodules are readily visualized in MR images as regions of attenuated signal intensity.

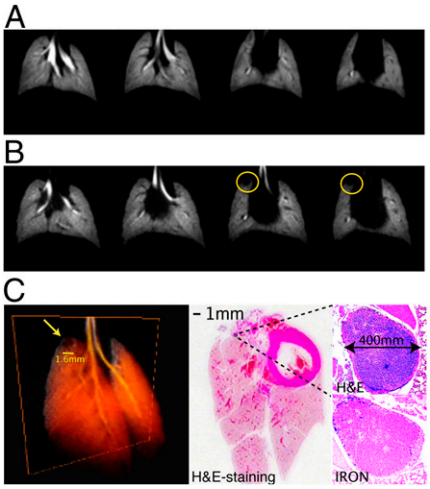

Fig. 2. Effect of SPION on HP ^{3}He images. (*A*) HP images (TE = 1 ms) from a control mouse that did not receive LHRH-SPION injection. (*B*) Images from a human prostate mouse model (TE = 1 ms) after injection of LHRH-SPIONs. Although the lung parenchyma is free of metastases, the iron uptake in the right cranial mediastinal lymph node caused by the i.p. injection produces a clear signal defect in the helium images (yellow circles). (*C*) 3D volume rendering of the HP helium image dataset. (*D*) H&E examination of the excised lung tissue (magnification, 1×). (*E*) Magnification (40×) of the same area, showing the lymph node and the iron uptake.

ted using HP ^{3}He MRI, by the signal voids they create. These voids can be distinguished from other signal voids, such as ventilation defects, because SPION-induced defects grow larger with TE. More challenging is their differentiation from signal voids caused by nearby blood vessels, especially if the SPION concentration is very small. Given these potentially confounding issues, it may be preferable in the future to acquire ^{3}He images before and after SPION administration, such that the difference can be unequivocally attributed to the presence of SPIONs. Such pre- and postcontrast imaging will also benefit from administering the particles i.v. rather than i.p., which will enable targeting to take place more quickly (1 to 2 h) and to reduce signal voids caused by nonspecific lymphatic uptake.

This method seems to have exquisite sensitivity, although exactly quantifying the SPION concentration required to generate an effect will require more detailed modeling. Quantifying SPION concentration from their effects on imaging remains an area of active research, even for conventional proton-based detection (39). A key determinant of sensitivity is the high SNR and resolution with which ^{3}He images of the lung can be acquired, providing a strong signal pool against which to observe the SPION contrast. However, the sensitivity is further enhanced by the ability to acquire ^{3}He

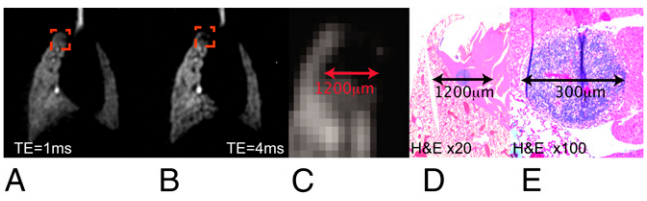

Fig. 3. Detection sensitivity. (*A*) HP ^{3}He lung images from a prostate tumor model mouse at TE = 1 ms. (*B*) Same image slice at TE = 4 ms. The signal loss in the right cranial lobe, due to the nonspecific iron uptake in the right cranial mediastinal lymph node, is clearly enhanced at longer TE, where it reaches a size of 1.2 mm. (*C*) Magnification of the signal loss area (TE = 4 ms). (*D* and *E*) Magnification of the same area (20× and 100×) in the histologic slide, which reveals a lymph node of 300 μm.

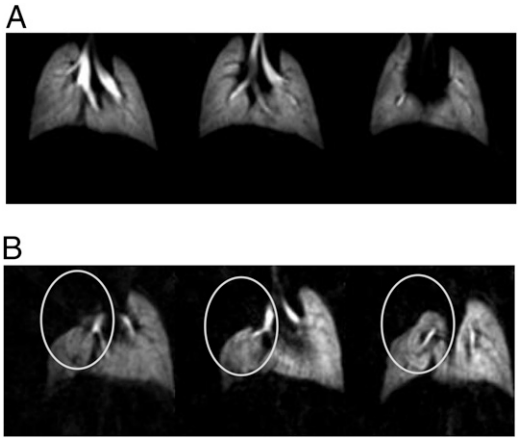

Fig. 4. Detection of pulmonary metastases in a breast adenocarcinoma mouse model. (*A*) HP images (TE = 4 ms) from a control mouse, showing normal ventilation patterns. (*B*) Images from a human breast adenocarcinoma mouse model (TE = 4 ms) after injection of LHRH-SPIONs. A clear signal defect can be seen in the right lobe (yellow circles). All of the HP ^{3}He lung MR images are formatted with 1-mm slice thickness.

images at relatively long TE, thereby enhancing the spatial blooming of the signal voids compared with what is achievable in the lung with proton MRI. The size of the signal void will increase with TE, but this is constrained by the T_2^* in the native lung. Because T_2^* is much longer for ^{3}He than for ^{1}H in the lung, ^{3}He can be imaged with a longer TE to make micrometastases visible well before they cause macroscopic morphologic changes in the lung parenchyma. On the basis of the example of SPION uptake in the right cranial mediastinal lymph node, this suggests that cancer lesions smaller than 300 μm in diameter are detectable and, with further optimization, even single cancer cells may become detectable. Although we have focused here on imaging of pulmonary metastases, the method could be readily extended with suitably functionalized SPIONS to permit noninvasive molecular characterization of primary lung nodules at a much earlier stage than current methods allow.

Clinical translation of the methods described here should also be feasible. HP ^{3}He lung MRI is already well demonstrated in human subjects, with images having a typical spatial resolution of $3 \times 3 \times 10$ mm^3 or higher acquired in a single breath hold (40). Moreover, a wide variety of SPION agents have already been demonstrated to be safe for clinical use and approved by the US Food and Drug Administration (17), and with suitable preclinical safety studies, the LHRH-SPIONs used in our studies could be administered to human subjects under an investigational new drug protocol. Although it is unlikely that the extraordinary sensitivity we have demonstrated in this preclinical study would be maintained in clinical imaging, the present data and strong SPION blooming suggest that pulmonary nodules could be detected with molecular specificity at a resolution of <1 mm, which would far exceed the sensitivity of FDG-PET.

The proposed imaging method can also be used in conjunction with hyperpolarized ^{129}Xe, the supply of which is extracted from the atmosphere and is therefore virtually unlimited (unlike ^{3}He). ^{129}Xe MRI is now entering clinical trials, and it provides resolution similar to that of ^{3}He MRI (28). ^{29}Xe MRI may have different sensitivity to SPION contrast than ^{3}He. ^{129}Xe has a gyromagnetic ratio that is 2.75 times lower than that of ^{3}He, making it less sensitive to SPION gradients. However, its lower gyromagnetic ratio also increases the ^{129}Xe T_2^* in the native lung, permitting longer TE to be used to enhance SPION sensitivity. ^{129}Xe has also a much lower diffusion coefficient in the lung compared with ^{3}He, which

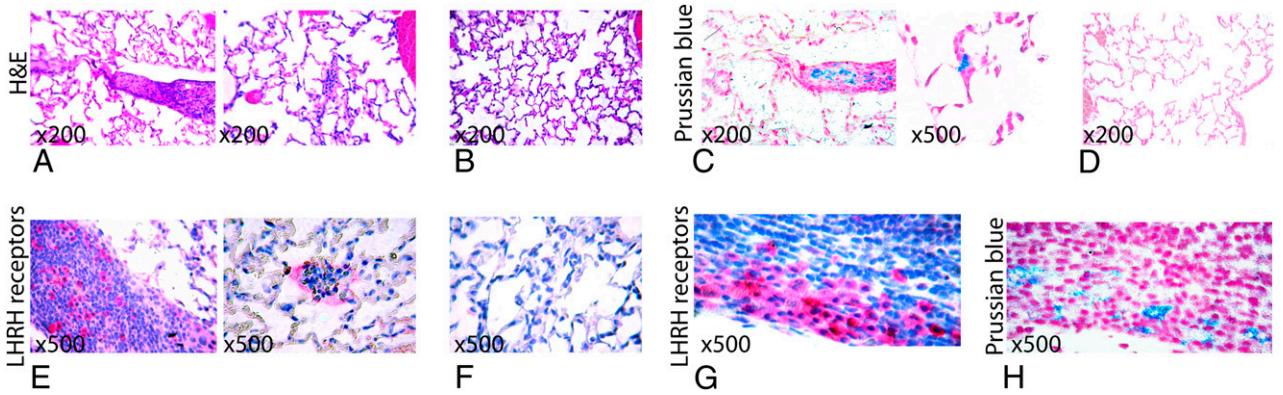

Fig. 5. Targeting of pulmonary micrometastases by LHRH-SPION. (*A*) H&E staining from the right cranial lobe showing medium-sized (*Left*) and very small (*Right*) micrometastases as regions of high cell density and marked overlapping of nuclei. (*B*) H&E staining from the right lung lobe showing normal lung parenchyma. (*C*) Prussian blue staining showing positive uptake of LHRH-SPION (bright blue) by the cancer cells in the lung parenchyma. (*D*) Prussian blue staining showing absence of iron in the healthy lung parenchyma. (*E*) Immunohistochemical analyses of LHRH receptors, showing LHRH receptor expression (bright pink) in the cancer metastases in the lung parenchyma. (*F*) Immunohistochemical analyses of LHRH receptors, showing absence of LHRH receptors in the healthy lung parenchyma. (*G*) Immunohistochemical analyses of LHRH receptors, showing LHRH receptors in a lung parenchyma micrometastases, with Prussian blue staining (*H*) of the same tissue showing positive iron uptake. All pictures are captured under the same magnification (500×) unless otherwise indicated.

could make it more susceptible to SPION dephasing by preventing the alveolar-level spin phase averaging due to diffusion.

For the present work, we chose LHRH-functionalized SPIONs because the LHRH receptor is overexpressed in such a wide variety of human cancers (41) and because these particles are taken up and trapped with remarkably high efficiency in metastatic cancer cells in the lung. However, the imaging approach described here would be equally compatible with a wide variety of other types of labeled SPIONs that have been developed in recent years, including those targeted to $\alpha_v\beta_3$ (42), HER2-nu (43), folate (44), and EGF (45) receptors. In particular, particles targeted to EGF receptors could be promising for early detection of lung cancer foci in high-risk patients (46).

Although much work remains to understand the potential clinical role of the imaging method described here, its value must eventually derive from very high specificity combined with high detection sensitivity. For example, if a patient with a confirmed primary tumor receives an x-ray CT scan that reveals small (<5 mm) pulmonary nodules, there is currently no means to evaluate whether these nodules are benign or metastatic. Such nodules are too small for biopsy and are below the detection threshold of FDG-PET. However, if this patient could receive an HP gas MRI scan before and after administration of SPIONs targeted to their primary tumor type, it could be immediately established whether the primary tumor had metastasized to the lung, and the patient could be administered the right therapy without delay. Ideally, the method could also be used to track the response of metastases to therapy, although this will require a more detailed understanding of the clearance of these particles. Because the LHRH-SPIONs are not metabolized by the cancer cells, their effect is expected to persist unless the cell undergoes apoptosis or division (47).

Finally, the combination of labeled magnetic nanoparticles and HP gas MRI is not limited to cancer detection and monitoring but can also provide a means for MRI of other important molecular processes in the lungs. More generally, the method provides the ability to label cells and track their fate noninvasively in the lungs—a task that has historically been quite difficult. For example, the basic methodology enables tracking of cancer cells to provide insights into oncogenic pathways and vulnerability to metastatic invasion, or in the area of asthma for tracking of T cells to enhance understanding of their recruitment and airway infiltration. This remarkably sensitive and specific imaging method promises to advance diverse areas, such as cancer imaging, drug development and delivery, and lung biology.

Materials and Methods

^{3}He Polarization. ^{3}He was polarized by a prototype commercial polarizer (IGI.9600.He; Magnetic Imaging Technologies). The system optically pumps the D_1 electronic transition of rubidium vapor to create a high level of ground state electron spin polarization, which is converted into ^{3}He nuclear polarization through collisions between the rubidium and helium atoms. The system produces 1.2 L of ^{3}He (Spectra Gases) typically polarized overnight, with a time constant of ≈5 h, to ≈30%. After ^{3}He polarization, the optical cell was cooled to room temperature, and the ^{3}He was dispensed into a 150-mL or 300-mL Tedlar bag (Jensen Inert Products) housed in a Plexiglas cylinder. The cylinder was then attached to an HP gas-compatible ventilator located ≈1 m from the opening of the 2-T magnet, where the longitudinal ^{3}He relaxation (26) is ≈20 min, allowing imaging to be performed with acceptable SNR for approximately that duration.

HP ^{3}He MRI. Images were acquired on a 2-T superconducting magnet with a horizontal 30-cm clear bore (Oxford Instruments) equipped with 18 G/cm shielded gradients (Resonance Research), controlled by a GE EXCITE 12.0 console (GE Healthcare). The scanner was interfaced to the dual-tuned (85.1/64.8 MHz) birdcage coil (5.5 × 3.5 cm) using a separate integrated transmit/receive switch with 31-dB gain preamplifier (Nova Medical) for the ^{1}H or ^{3}He frequency. These frequencies were created by modifying the intrinsic 63.86-MHz frequency of the scanner to either 85.1 MHz for ^{1}H or 64.8 MHz for ^{3}He using an up–down converter (Cummings Electronics Labs).

The imaging protocol started with a standard ^{1}H gradient echo MRI to localize the chest cavity. High-resolution 3D HP ^{3}He images (156-μm isotropic resolution) were then acquired with a 2-cm field of view (FOV) in both the coronal and sagittal planes using a 3D radial encoding scheme. Image acquisition used an axial slab excitation matching the 2-cm FOV to mitigate wraparound artifacts from ^{3}He in the trachea. The first, short TE images (TE = 1 ms) were acquired with TE/repetition time (TR) = 1/5 ms, a constant flip angle of 13°, 20 radial k-space views per breath, and 31.25-kHz bandwidth. Long TE images (TE = 4 ms) were acquired using TE/TR = 4/8 ms, a flip angle of 17°, and 12 k-space views per breath. After accumulating 20,001 radial k-space views, the data were regridded on a 128 × 128 × 128 Cartesian matrix and Fourier-transformed to give images with a 156 × 156 × 156 μm^3 Nyquist-limited isotropic resolution.

Animal Care and Use. All experiments were performed according to the guidelines of a Duke University Institutional Animal Care and Use Committee–approved protocol. For these experiments, female and male athymic nude mice (Ncr nu/nu), 5 to 6 weeks of age (Charles River Laboratory), were housed in sterile cages and fed autoclaved chow and water ad libitum. Four male mice were inoculated subcutaneously in the flank with Pc-3 human prostate cancer cells suspended in GFR-Matrigel (BD Biosciences), a basement membrane

protein matrix known to improve early angiogenesis. Eight female mice were inoculated with MDA-MB-231 and MDA-MB-435s breast cancer cells, also suspended in GFR-Matrigel. Four mice were inoculated with MDA-MB-231 in the mammary fat pads, whereas the other four were inoculated with MDA-MB-435s subcutaneously in the shoulder.

Mice were selected to undergo imaging when the primary tumor reached a size of ≈1 cm^3. Approximately 24–48 h before imaging, the selected mouse received an i.p. injection by 27-gauge needle of 100 mg/kg LHRH-SPION suspended in saline. The suspension was prepared as described in refs. 48 and 49 using a cell homogeneizer to reduce SPION agglomeration and was sonicated for 10 min in a bath of ice and water before injection.

Before imaging, the animals were anesthetized with an i.p. injection of pentobarbital (3 mg/kg of body weight), and anesthesia was maintained during the imaging by repeated i.p. injection of pentobarbital, as needed. A tracheotomy was performed to insert a 24-gauge tracheal tube that extended to 2 to 3 mm above the carina. The tracheal tube was secured by sutures and connected to a low-dead volume Y-connector separating the inhalation and exhalation lines of an MR-compatible constant volume ventilator. The mouse was ventilated with a mixture of 20% oxygen and 80% ^{3}He gas in the supine position at 100 breaths per minute with a 0.2-mL tidal volume. The airway pressure and echocardiogram of the animal were continuously monitored throughout the study. Body temperature was monitored by a rectal temperature probe and maintained at ≈37 °C by warm air passing through the magnet bore.

Histology. At the end of the MRI sessions, the animals were killed, and the lungs were excised, fixed in 10% neutral-buffered formalin, and individually embedded in single paraffin blocks. Each paraffin block was then completely sectioned at 5 μm every 200 μm using a microtome and mounted on glass slides. Groups of three adjacent slides were then stained with H&E, Perl Prussian blue, or used for immunohistochemistry (IHC) analysis. Adjacent IHC and H&E slides were then examined under a light microscope to identify and locate small metastases, whereas Perl Prussian blue staining for iron was used to detect SPION uptake. For IHC analysis, tissue sections were incubated with a mouse monoclonal primary antibody raised against human gonadotropin-releasing hormone receptor (clone A9E4, VP-G811; Vector Laboratories,) in a 1:20 dilution for 30 min. Primary antibody binding was then determined using the Mach 4 Universal Polymer Detection kit (catalog no. M4U536H; Biocare Medical) and visualized using Vulcan Fast Red Chromagen (Biocare Medical).

ACKNOWLEDGMENTS. We thank Prof. Laurence Hedlund for help with our animal protocols; Abraham Thomas for involvement in the first set of imaging experiments; Dr. Zuowei Su for the immunohistochemistry analysis; Sally Zimney for assistance in preparation of the manuscript; NCI Cancer Research Imaging Camp for providing adenocarcinoma mouse models; and Dr. Michael Foster for comments on the manuscript. This work was supported by National Institutes of Health Grants R01 EB02122 and P41 RR005959, National Cancer Institute Grant U24 CA092656, and the Duke Comprehensive Cancer Center.

1. American Cancer Society, Cancer facts & Figures 2009, http://www.cancer.org/downloads/STT/500809web.pdf.
2. Engel J, et al. (2003) The process of metastasisation for breast cancer. *Eur J Cancer* 39: 1794–1806.
3. Hess KR, et al. (2006) Metastatic patterns in adenocarcinoma. *Cancer* 106:1624–1633.
4. Coleman RE (1999) PET in lung cancer. *J Nucl Med* 40:814–820.
5. Kennel SJ, et al. (2000) High resolution computed tomography and MRI for monitoring lung tumor growth in mice undergoing radioimmunotherapy: correlation with histology. *Med Phys* 27:1101–1107.
6. Gambhir SS (2002) Molecular imaging of cancer with positron emission tomography. *Nat Rev Cancer* 2:683–693.
7. Harris RS, Schuster DP (2007) Visualizing lung function with positron emission tomography. *J Appl Physiol* 102:448–458.
8. Frush DP, Applegate K (2004) Computed tomography and radiation: understanding the issues. *J Am Coll Radiol* 1(2):113–119.
9. Deroose CM, et al. (2007) Multimodality imaging of tumor xenografts and metastases in mice with combined small-animal PET, small-animal CT, and bioluminescence imaging. *J Nucl Med* 48:295–303.
10. Bulte JWM, Brooks RA, Moskowitz BM, Bryant LH, Jr, Frank JA (1999) Relaxometry and magnetometry of the MR contrast agent MION-46L. *Magn Reson Med* 42: 379–384.
11. Mendonca Dias MH, Lauterbur PC (1986) Ferromagnetic particles as contrast agents for magnetic resonance imaging of liver and spleen. *Magn Reson Med* 3:328–330.
12. Bulte JWM, Kraitchman DL (2004) Iron oxide MR contrast agents for molecular and cellular imaging. *NMR Biomed* 17:484–499.
13. Rogers WJ, Meyer CH, Kramer CM (2006) Technology insight: In vivo cell tracking by use of MRI. *Nat Clin Pract Cardiovasc Med* 3:554–562.
14. Shapiro EM, et al. (2004) MRI detection of single particles for cellular imaging. *Proc Natl Acad Sci USA* 101:10901–10906.
15. Wang YX, Hussain SM, Krestin GP (2001) Superparamagnetic iron oxide contrast agents: Physicochemical characteristics and applications in MR imaging. *Eur Radiol* 11: 2319–2331.
16. Gupta AK, Gupta M (2005) Synthesis and surface engineering of iron oxide nanoparticles for biomedical applications. *Biomaterials* 26:3995–4021.
17. Corot C, Robert P, Idée JM, Port M (2006) Recent advances in iron oxide nanocrystal technology for medical imaging. *Adv Drug Deliv Rev* 58:1471–1504.
18. Brudin LH, Rhodes CG, Valind SO, Wollmer P, Hughes JM (1987) Regional lung density and blood volume in nonsmoking and smoking subjects measured by PET. *J Appl Physiol* 63:1324–1334.
19. Hatabu H, Alsop DC, Listerud J, Bonnet M, Gefter WB (1999) T2* and proton density measurement of normal human lung parenchyma using submillisecond echo time gradient echo magnetic resonance imaging. *Eur J Radiol* 29:245–252.
20. Kuethe DO, Adolphi NL, Fukushima E (2007) Short data-acquisition times improve projection images of lung tissue. *Magn Reson Med* 57:1058–1064.
21. van Beek EJR, et al. (2004) Functional MRI of the lung using hyperpolarized 3-helium gas. *J Magn Reson Imaging* 20:540–554.
22. de Lange EE, et al. (1999) Lung air spaces: MR imaging evaluation with hyperpolarized 3He gas. *Radiology* 210:851–857.
23. Salerno M, et al. (2001) Hyperpolarized noble gas MR imaging of the lung: Potential clinical applications. *Eur J Radiol* 40:33–44.
24. Guenther D, Hanisch G, Kauczor HU (2000) Functional MR imaging of pulmonary ventilation using hyperpolarized noble gases. *Acta Radiol* 41:519–528.
25. Fain SB, et al. (2007) Functional lung imaging using hyperpolarized gas MRI. *J Magn Reson Imaging* 25:910–923.
26. Driehuys B, et al. (2007) 3He MRI in mouse models of asthma. *Magn Reson Med* 58: 893–900.
27. Dugas JP, Garbow JR, Kobayashi DK, Conradi MS (2004) Hyperpolarized (3)He MRI of mouse lung. *Magn Reson Med* 52:1310–1317.
28. Driehuys B, Hedlund LW (2007) Imaging techniques for small animal models of pulmonary disease: MR microscopy. *Toxicol Pathol* 35:49–58.
29. Takahashi M, Kubo S, Kiryu S, Gee J, Hatabu H (2007) MR microscopy of the lung in small rodents. *Eur J Radiol* 64:367–374.
30. Walker TG, Happer W (1997) Spin-exchange optical pumping of noble-gas nuclei. *Rev Mod Phys* 69:62–642.
31. Mugler JP, et al. (2009) T2* for Hyperpolarized Xe129 in the Healthy Human Lung at 1.5T and 3T. International Society of Magnetic Resonance in Medicine. Seventeenth Meeting Proceedings (ISMRM, Berkeley, CA), p. 2207.
32. Salerno M, Brookeman JR, de Lange EE, Mugler JP, 3rd (2005) Hyperpolarized 3He lung imaging at 0.5 and 1.5 Tesla: A study of susceptibility-induced effects. *Magn Reson Med* 53:212–216.
33. Pintaske J, Müller-Bierl B, Schick F (2006) Geometry and extension of signal voids in MR images induced by aggregations of magnetically labelled cells. *Phys Med Biol* 51: 4707–4718.
34. Viallon M, et al. (2000) Laser-polarized (3)He as a probe for dynamic regional measurements of lung perfusion and ventilation using magnetic resonance imaging. *Magn Reson Med* 44:1–4.
35. Leuschner C, et al. (2006) LHRH-conjugated magnetic iron oxide nanoparticles for detection of breast cancer metastases. *Breast Cancer Res Treat* 99:163–176.
36. Welch DR (1997) Technical considerations for studying cancer metastasis in vivo. *Clin Exp Metastasis* 15:272–306.
37. Leuschner C, Enright FM, Gawronska-Kozak B, Hansel W (2003) Human prostate cancer cells and xenografts are targeted and destroyed through luteinizing hormone releasing hormone receptors. *Prostate* 56:239–249.
38. Shibata S, et al. (2007) The time course of lymphatic routes emanating from the peritoneal cavity in rats. *Anat Histol Embryol* 36:78–82.
39. Heyn C, Bowen CV, Rutt BK, Foster PJ (2005) Detection threshold of single SPIO-labeled cells with FIESTA. *Magn Reson Med* 53:312–320.
40. van Beek EJR, Wild JM (2005) Hyperpolarized 3-helium magnetic resonance imaging to probe lung function. *Proc Am Thorac Soc* 2:528–532, 510.
41. Schally AV, Nagy A (1999) Cancer chemotherapy based on targeting of cytotoxic peptide conjugates to their receptors on tumors. *Eur J Endocrinol* 141:1–14.
42. Zhang C, et al. (2007) Specific targeting of tumor angiogenesis by RGD-conjugated ultrasmall superparamagnetic iron oxide particles using a clinical 1.5-T magnetic resonance scanner. *Cancer Res* 67:1555–1562.
43. Artemov D, Mori N, Ravi R, Bhujwalla ZM (2003) Magnetic resonance molecular imaging of the HER-2/neu receptor. *Cancer Res* 63:2723–2727.
44. Choi H, Choi SR, Zhou R, Kung HF, Chen IW (2004) Iron oxide nanoparticles as magnetic resonance contrast agent for tumor imaging via folate receptor-targeted delivery. *Acad Radiol* 11:996–1004.
45. Yang L, et al. (2009) Single chain epidermal growth factor receptor antibody conjugated nanoparticles for in vivo tumor targeting and imaging. *Small* 5:235–243.
46. Suzuki M, et al. (2005) Epidermal growth factor receptor expression status in lung cancer correlates with its mutation. *Hum Pathol* 36:1127–1134.
47. Heyn C, et al. (2006) In vivo MRI of cancer cell fate at the single-cell level in a mouse model of breast cancer metastasis to the brain. *Magn Reson Med* 56:1001–1010.
48. Kumar CS, et al. (2004) Efficacy of lytic peptide-bound magnetite nanoparticles in destroying breast cancer cells. *J Nanosci Nanotechnol* 4:245–249.
49. Zhou J, Leuschner C, Kumar C, Hormes JF, Soboyejo WO (2006) Sub-cellular accumulation of magnetic nanoparticles in breast tumors and metastases. *Biomaterials* 27:2001–2008.